Supporting Information

Molecular engineering of D-Glucuronamide additive directs (100)-oriented Zn deposition for ultra-stable zinc-ion batteries

Le Zhang[a], Shuyu Bi[a], Xijun Liu[a], Qiangchao Sun[a], Tao Hu[a], Xionggang Lu[a], Hongwei Cheng[a,*]

[a] School of Materials Science and Engineering & State Key Laboratory of Advanced Refractories, Shanghai University, Shanghai 200444, P. R. China

Corresponding author: hwcheng@shu.edu.cn (H.W. Cheng)

Experimental Section

Preparation of electrolytes: Erythritol (Eth), DL-xylose (Xyl) and D-Glucuronamide (D-Glu) were purchased from Shanghai Macklin Biochemical Technology Co., Ltd. 2 M $ZnSO_4$ (ZS) electrolyte was prepared by dissolving zinc sulfate heptahydrate ($ZnSO_4 \cdot 7H_2O$, 99.995% Aladdin) into the deionized water. add various additives (Eth, Xyl, D-Glu) to ZS solution as modified electrolyte. Furthermore, add different amounts of D-Glucuronamide (D-Glu, 99%, Macklin) to the ZS solution to prepare ZS+D-Glux, where x = 5/10/20 mg mL^{-1}. If not mentioned, ZS+D-Glu refers to ZS+D-Glu10 and the addition amounts of Eth and Xyl additives were both 10 mg mL^{-1}.

Synthesis of $NH_4V_4O_{10}$: $NH_4V_4O_{10}$ (NVO) powder was prepared according to the previous reference.[1] A typical synthesis procedure involved dissolving 1.17 g of NH_4VO_3 (Aladdin, 99.0 wt.%) in 70 mL deionized water at 80 °C to form a yellow solution. Subsequently, 1.89 g of $H_2C_2O_4 \cdot 2H_2O$ (Aladdin, 99.0 wt.%) was added to the stirred solution under vigorous mechanical agitation. The mixture was maintained at 80 °C with continuous stirring for an additional 30 minutes. The reaction mixture was then transferred to a 100 mL Teflon-lined stainless-steel autoclave, sealed, and heated at 140 °C in an oven for 48 hours. Upon cooling to room temperature, the product was filtered, washed sequentially with deionized water (3×), and dried overnight at 60 °C to yield the final NVO material.

Preparation of $NH_4V_4O_{10}$ cathode: The NVO, acetylene black, and PVDF (20 mg mL^{-1}) were mixed in N-Methyl pyrrolidone (NMP) at a weight ratio of 8: 1: 1. The resulting slurry was then uniformly coated onto a 12 mm diameter carbon paper substrate using a doctor blade technique with a mass loading of 2–3 mg cm^{-2} and dried in a vacuum oven at 60 °C for 12 h to obtain NVO cathode.

Fabrications of Zn//Cu asymmetric cells, Zn//Zn symmetric cells and Zn//$NH_4V_4O_{10}$ full cells: CR2016 coin cells were assembled in an open-air environment. The Zn||Zn symmetrical cells and Zn||Cu asymmetric cells were assembled using a glass fiber film (Whatman GF/F, GE Healthcare) as the separator, and ZS or with different additives (Eth, Xyl, D-Glu) was used as the electrolyte. The Zn||NVO full cells were assembled with Zn foil as anode, the as-fabricated electrode (NVO) as a cathode, and ZS or ZS+D-Glu as the electrolyte. Each coin cell was filled with ~100 μL of electrolyte.

Electrochemical Measurements: Galvanostatic charge/discharge (GCD) curves, coulombic efficiency (CE) and battery performance were carried out on a battery test system (NEWARE, CT-4008TN-5V50mA, Shenzhen, China). The charge and discharge voltage range for the Zn||NVO was from 0.3 to 1.4 V. Chronoamperometry (CA), Linear sweep voltammetry (LSV), and Tafel plots (Tafel) were carried out on an electrochemical workstation (CHI760E, Shanghai Chenhua Instruments Co., Ltd.). The current-time transient curves were collected by CA measurement under an overpotential of −150 mV for 300 s. The LSV and Tafel were recorded using a three-electrode system, with a Pt mesh counter electrode, an Ag/AgCl reference electrode, and a Zn plate working electrode. LSV curves were collected from -1.0 to -1.9 V with a scan rate of 1.0 mV s^{-1} using 1 M Na_2SO_4 and 1 M Na_2SO_4 with different additives (Eth, Xyl, D-Glu) as electrolytes. Tafel were recorded from -0.8 to -1.1 V at a sweep rate of 5 mV s^{-1} in ZS/ZS+D-Glu electrolytes.
The Zn-based anode utilization (depth of discharge, DOD) severely impairs the feasibility of functional electrolytes under strictly practical conditions, as described by the following equation (Eqs. 1):[2,3]

$$DOD = \frac{y}{C_{Zn,volume} \cdot x \cdot 10^{-4}} \times 100\% = y / 0.585x \times 100\% \qquad \text{* MERGEFORMAT (1)}$$

Where y (mAh cm^{-2}) represents the Zn areal capacity used in electrochemical testing，x (μm) is the thickness of Zn foil, and $C_{Zn,\ volume}$ is the theoretical volume capacity of zinc.

The Arrhenius activation energy (E_a) was calculated using the equation (Eqs. 2):[4]

$$\frac{1}{R_{ct}} = A \cdot exp \cdot (-\frac{E_a}{RT}) \quad \text{* MERGEFORMAT (2)}$$

In this case, R_{ct}, A, R, and T represent the interfacial resistance, frequency factor, gas constant, and temperature, respectively.

Electrochemical impedance spectroscopy (EIS) was recorded with a frequency range of 0.01 ~ 1,000,000 Hz. The D_{Zn}^{2+} can be calculated using the equation (Eqs. 3, 4):[5]

$$D = \frac{R^2T^2}{2A^2n^4F^4C^2\sigma^2} \quad \text{* MERGEFORMAT (3)}$$

$$Z' = \sigma \cdot \omega^{-1/2} \quad \text{* MERGEFORMAT (4)}$$

Where ω is the angular frequency, and σ can be calculated from the slope of the slope between Z' and $\omega^{-1/2}$. Besides, R is the universal gas constant, T is the absolute temperature, A is the surface area of the electrode, F is the Faraday constant, and C is the concentration of Zn^{2+}.

To obtain the apparent diffusion coefficient of electron transfer, D_{app}, the peak current i_p from cyclic voltammetry was plotted against the square root of scan rate, $v^{1/2}$. Then, D_{app} was obtained using the Randles-Sevcik equation (Eqs. 5):[6]

$$i_p = 0.4463 \cdot nFAC\sqrt{\frac{nF\nu D_{app}}{RT}} \quad \text{* MERGEFORMAT (5)}$$

Where i_p is the peak current (A), n is the number of electrons transferred in the redox event (n = 2 for each redox step), F is Faraday's constant (96,485 $C \cdot mol^{-1}$), A is the electrode area (cm^2), C is the concentration of the redox species (mol/cm^3), v is the scan rate ($V\ s^{-1}$), D_{app} is the diffusion coefficient ($cm^2\ s^{-1}$), R is the universal gas constant (8.314 $J \cdot K^{-1} \cdot mol^{-1}$) and T is the absolute temperature (K).

The homogeneous electron self-exchange rate constant K_{ex} can be calculated from the Dahms-Ruff equation (Eqs. 6):[6]

$$D_{app} = \frac{1}{6}C\delta^2K_{ex} \quad \text{* MERGEFORMAT (6)}$$

δ is the distance the electron and the proton move, which was estimated by $(N_AC)^{-1/3}$, where N_A is Avogadro's number). The specific capacity (C, mAh/g) was calculated according to the equation below (Eqs. 7):[6]

$$C = \frac{I \cdot \Delta t}{3.6 \times m} \quad \text{* MERGEFORMAT (7)}$$

Where I is the current density (mA), Δt is the time (s), m is the mass of the active materials (mg).

Materials Characterizations: The deposition and the cycled anodes morphologies were observed on a scanning electron microscope (SEM, JSM-7500F), laser confocal scanning microscope (LCSM, LSM900), and an optical microscope (CIS-0M-002). The electrolyte structure was evaluated by Raman spectroscopy (Raman, Jobin Yvon LabRAM HR800), Fourier transform infrared spectroscopy (FTIR, TENSOR 27), and proton nuclear magnetic resonance spectroscopy (^{1}H-NMR, AVANCE 500MHZ).The crystalline structures of Zn anodes and cathodes were analyzed by X-ray diffraction (XRD, D8 Advance) equipped with Cu Kα-radiation (λ=1.5418). The wettability of the Zn surface under different electrolytes was performed on the contact angle measurement (Theta Flex).

DFT Calculations: DFT calculations were conducted using the Vienna Ab Initio Simulation Package (VASP),[7,8] employing the generalized gradient approximation (GGA) with the Perdew-Burke-Ernzerhof (PBE) functional to handle exchange-correlation effects.[9] To model ionic cores and account for valence electrons, projected augmented wave (PAW) potentials were used alongside a plane-wave basis set with a kinetic energy cutoff of 520 eV.[10] A Gaussian smearing method with a width of 0.05 eV was applied to accommodate partial occupancies of Kohn-Sham orbitals. Self-consistency in electronic energy was deemed achieved when the change in energy fell below 1×10^{-5} eV. Geometry optimizations

were considered converged once the force on each atom was less than 0.01 eV/Å. Dispersion interactions were included via Grimme's DFT-D3 approach.[11] For Brillouin zone sampling, a Monkhorst-Pack k-point grid generated by VASPKIT with a precision of 0.04 was utilized for the lattice constant optimization, while maintaining a vacuum spacing of 15 Å perpendicular to the structure's plane to prevent spurious interactions between periodic images[12,13]. Finally, the adsorption energies (E_{ads}) were calculated as $E_{ads} = E_{ad/sub} - E_{ad} - E_{sub}$, where $E_{ad/sub}$, E_{ad}, and E_{sub} are the total energies of the optimized adsorbate/substrate system, the adsorbate in the structure, and the clean substrate, respectively.

MD simulations: The molecular dynamics (MD) simulations were performed using LAMMPS (Large-scale Atomic/Molecular Massively Parallel Simulator) to investigate the structural and dynamic properties of the system.[14] The initial configuration was generated using Packmol to pack molecules with appropriate spatial arrangements and avoid atomic overlaps.[15] The OPLS-AA (Optimized Potentials for Liquid Simulations - All Atom) force field was employed to describe bonded and non-bonded interactions with SPC/E water model and the corresponding atom charges were based on restrained electrostatic potential (RESP) charges with long-range electrostatic forces calculated using the PPPM (Particle-Particle Particle-Mesh) method.[16,17] Before dynamic simulations, the system was energy-minimized using the conjugate gradient algorithm to eliminate unfavorable atomic contacts. Subsequently, the system underwent equilibration under the NPT ensemble from 10 K to 298 K for 100 ps to relax the density, followed by 200 ps equilibration under NPT ensemble (under 1 atmosphere). A final NPT production run of 20 ns was conducted at 298 K with a 1 fs timestep for data collection. The SHAKE algorithm was applied to constrain hydrogen-involved bonds in water molecules, ensuring efficient integration. Temperature and pressure were regulated using the Nosé-Hoover thermostat and barostat, respectively. Trajectories were recorded every 1 ps for post-simulation analysis, including radial distribution function (RDF) calculations to examine intermolecular interactions.

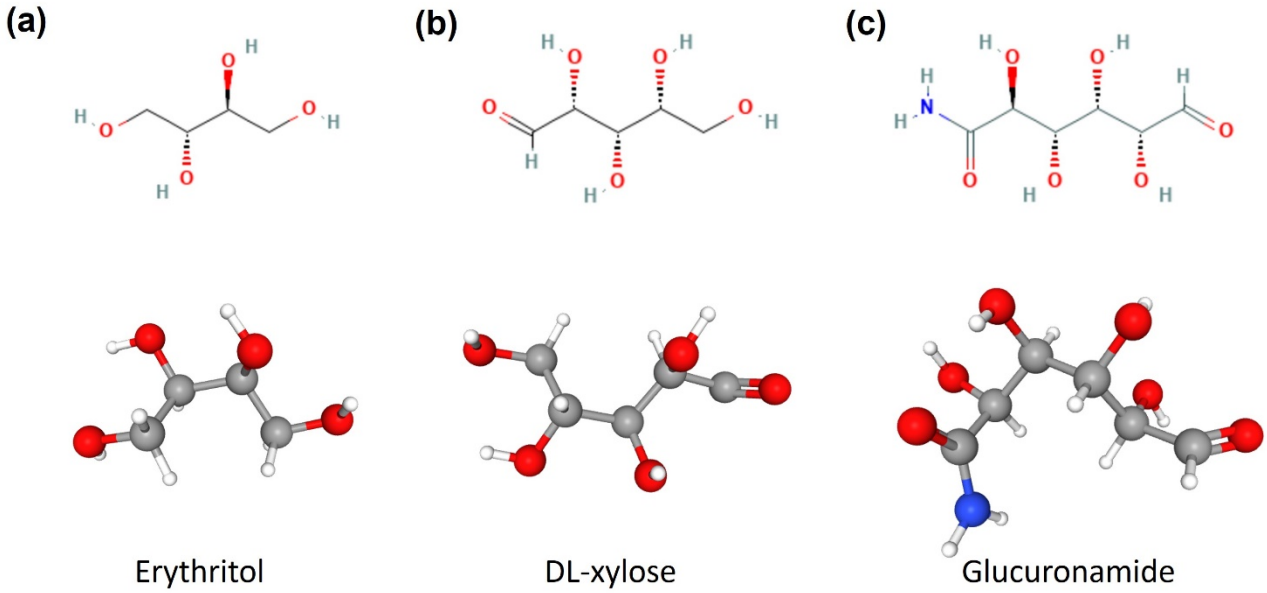

Fig. S1. Molecular structure of Erythritol (Eth), DL-xylose (Xyl) and D-Glucuronamide (D-Glu).

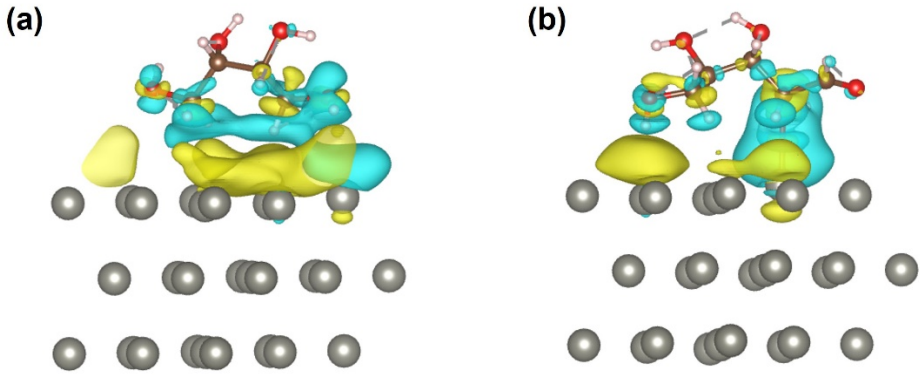

Fig. S2. The 3D charge density difference of (a) Eth and (b) Xyl on the Zn (002) plane (The yellow and cyan iso-surfaces represent the increase and decrease in electron density, respectively).

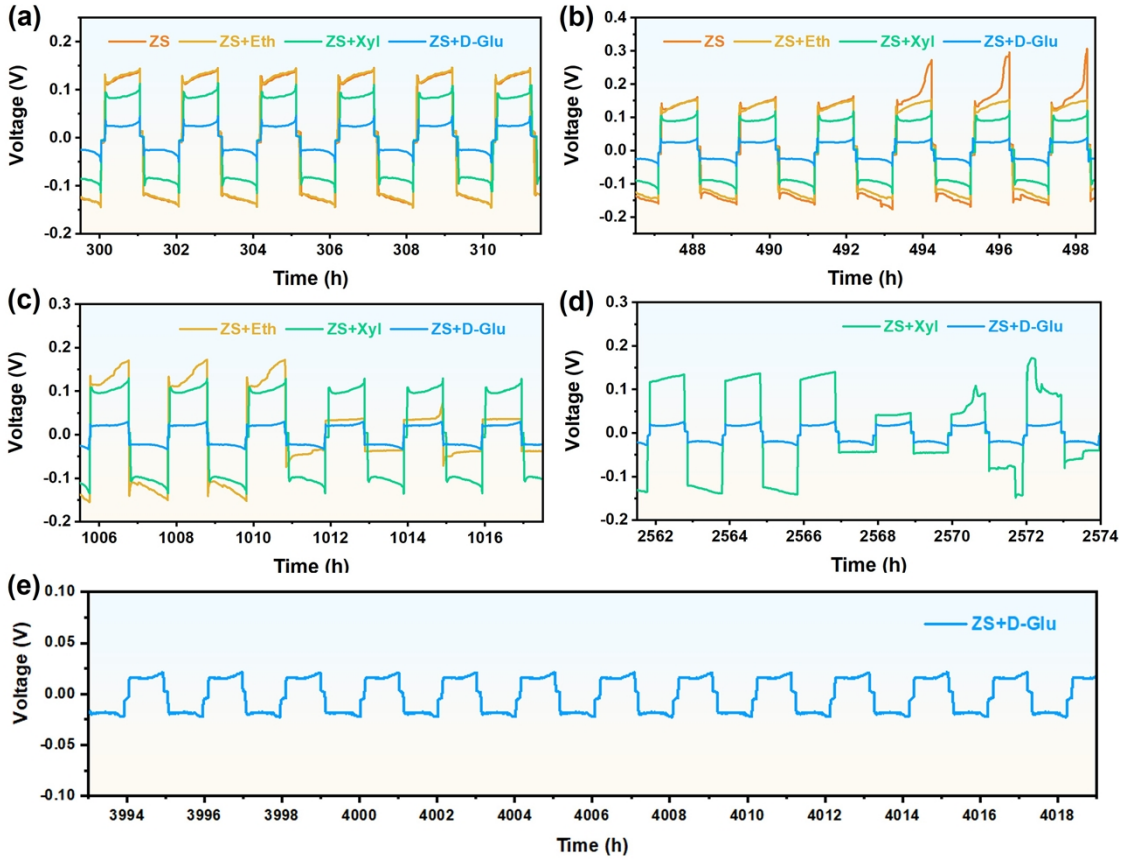

Fig. S3. The detailed voltage profiles at different cycle time ranges.

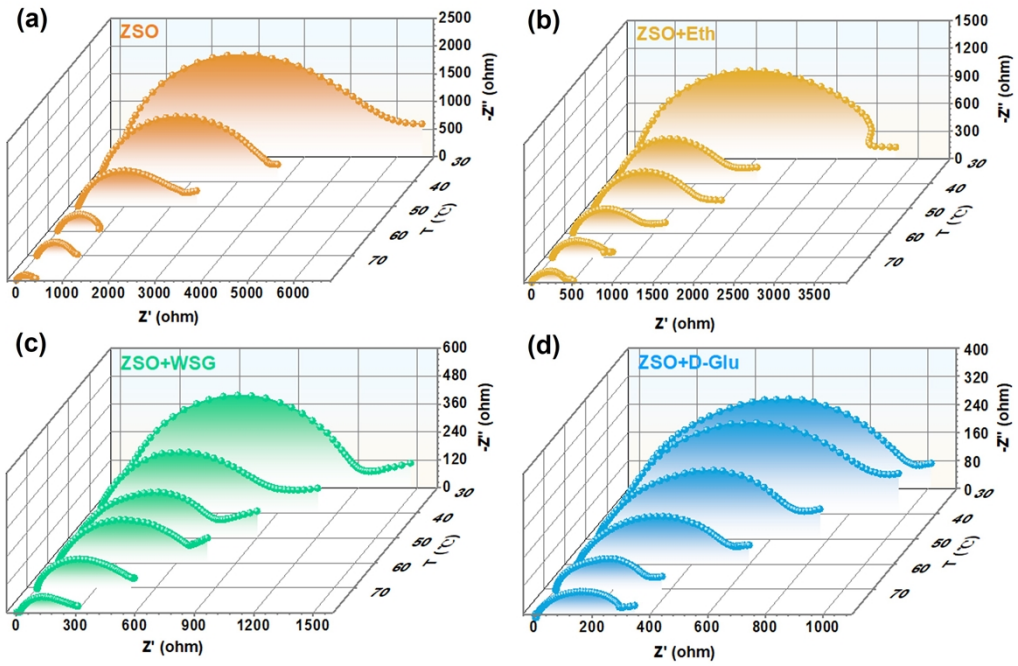

Fig. S4. Temperature-dependent electrochemical impedance spectra of Zn||Zn symmetric batteries using (a) ZS, (g) ZS+Eth, (c) ZS+Xyl, (g) ZS+D-Glu electrolytes.

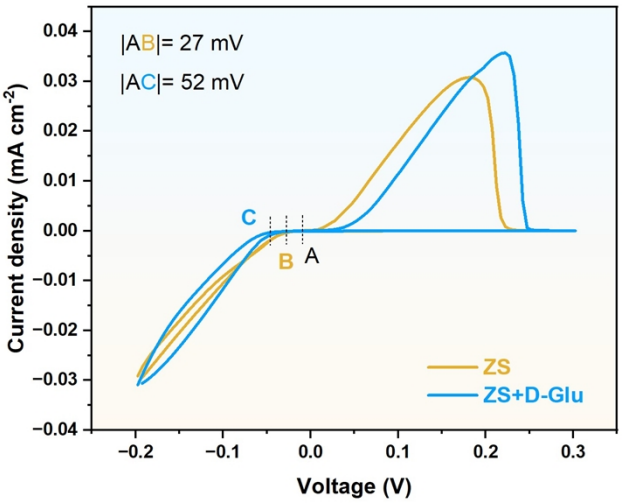

Fig. S5. CV curves of Zn metal in ZS/ZS with different additives electrolyte.

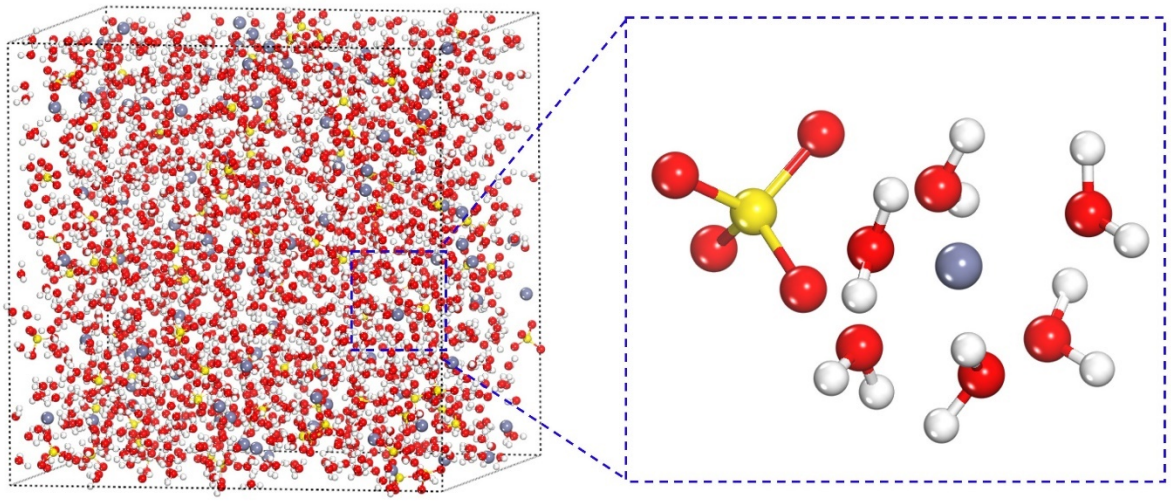

Fig. S6. MD simulation snapshots of the ZS electrolytes and the local solvation structure of hydrated Zn^{2+}.

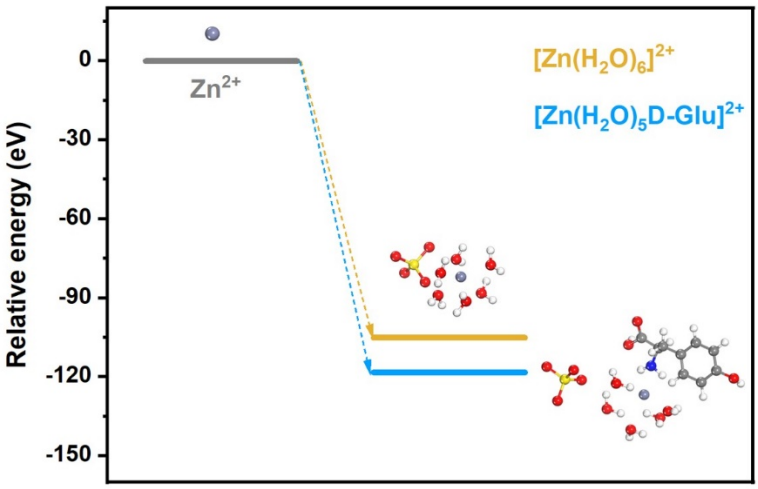

Fig. S7. Relative energies for $[Zn(H_2O)_6]^{2+}$ and $[Zn(H_2O)_5\,D\text{-}Glu]^{2+}$.

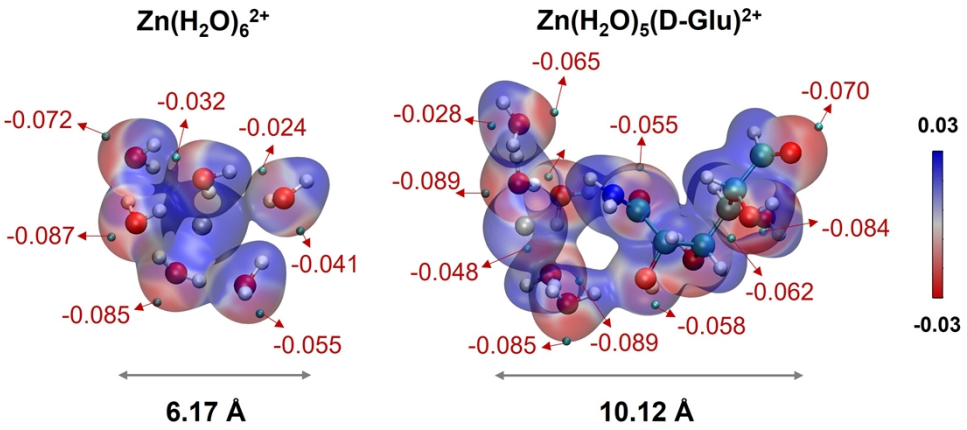

Fig. S8. Electrostatic potential mapping and sizes of solvated Zn^{2+} in the ZS and ZS+D-Glu electrolytes.

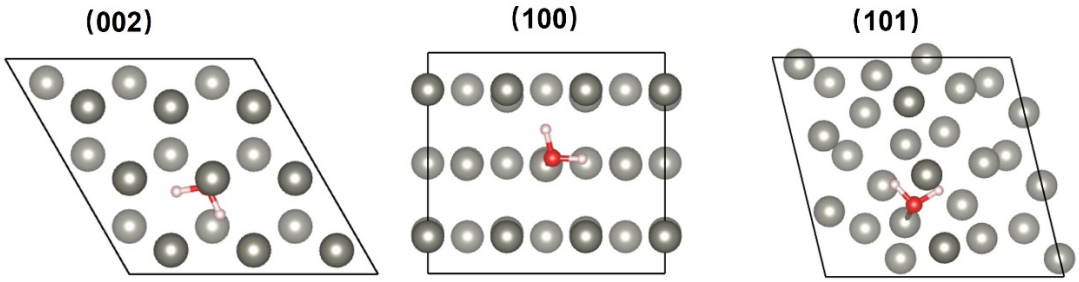

Fig. S9. Schemes showing H_2O molecule adsorbed on the Zn (002), (100), and (101) surfaces.

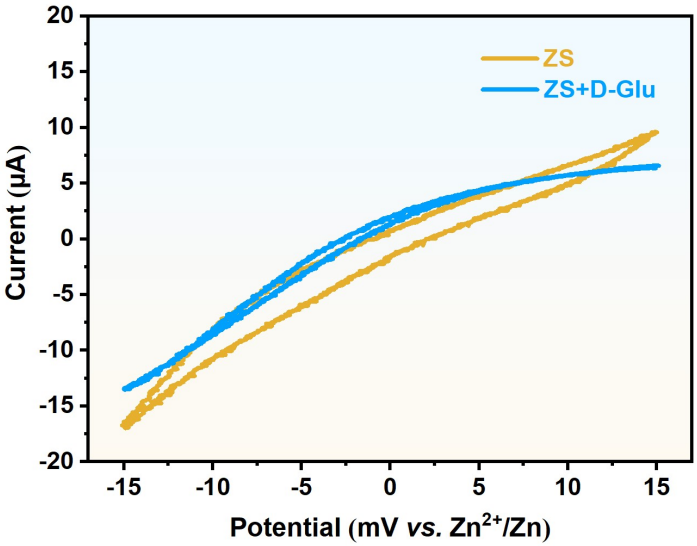

Fig. S10. CV curves for Zn||Zn cells from -15 mV to 15 mV.

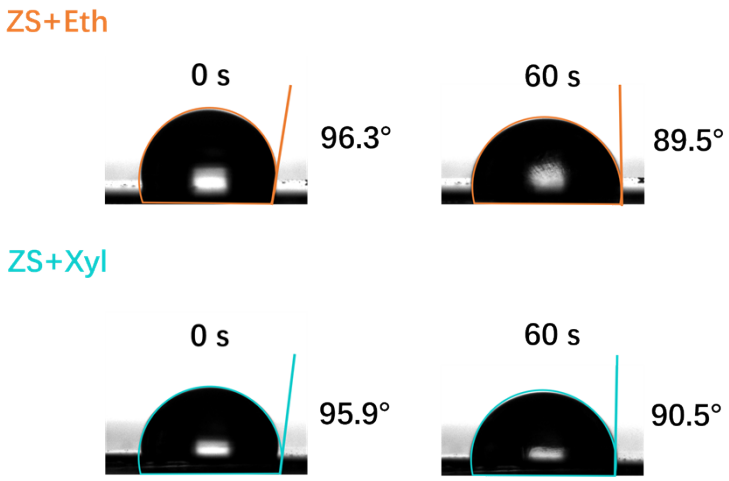

Fig. S11. Contact angle measurement of ZS+Eth and ZS+Xyl droplets on the Zn surface.

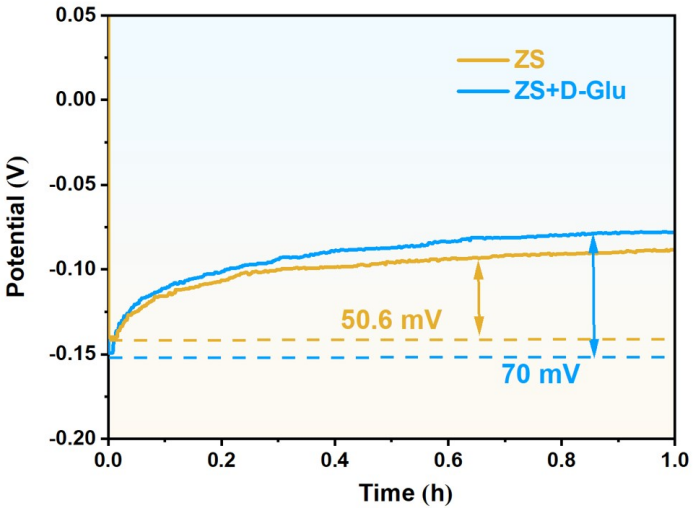

Fig. S12. Nucleation overpotential based on the Ti foils in ZS and ZS+D-Glu electrolytes at 2 mA cm^{-2}.

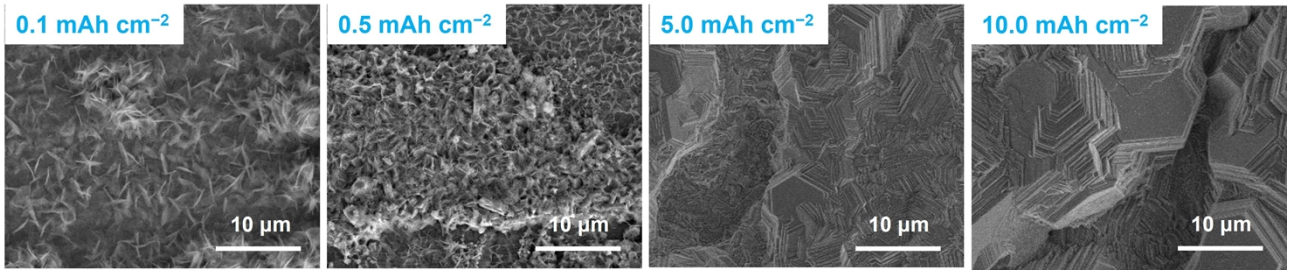

Fig. S13. SEM images of Zn electrodeposits in ZS with 0.1 mAh cm^{-2}, 0.5 mAh cm^{-2}, 5.0 mAh cm^{-2}, and 10.0 mAh cm^{-2} plating capacities.

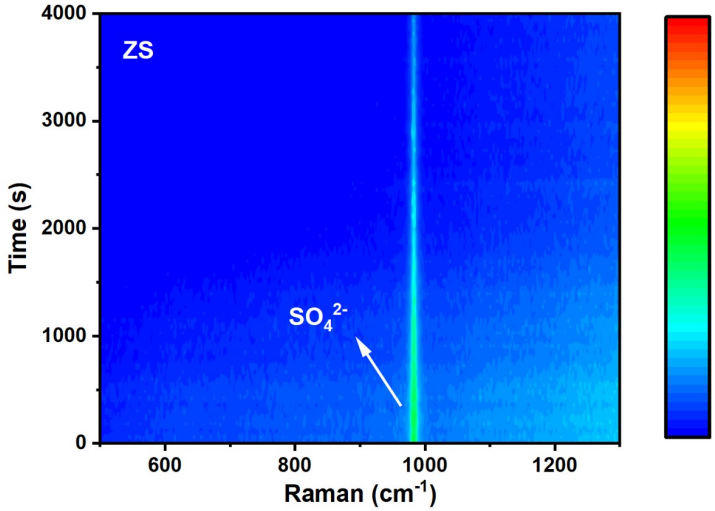

Fig. S14. *In-situ* Raman spectrum for Zn anode tested in ZS and ZS+D-Glu electrolytes in Zn^{2+} plating process.

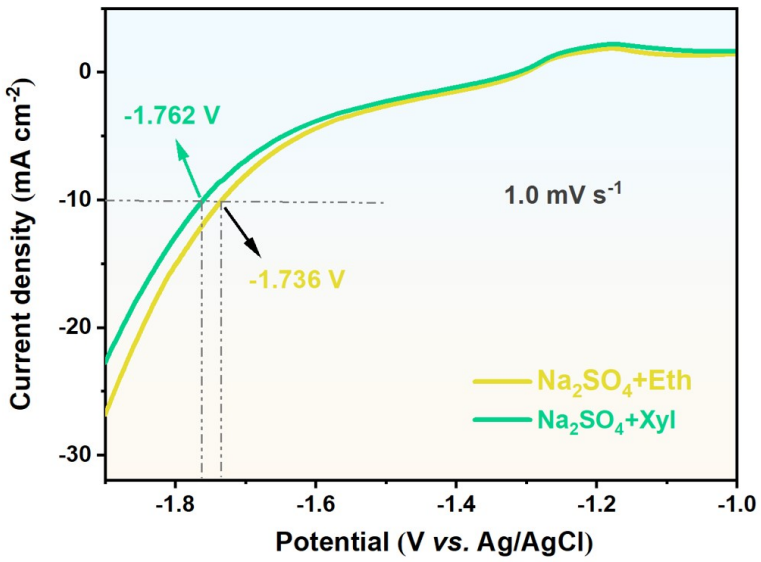

Fig. S15. LSV for the Zn anode at a scan rate of 1.0 mV s^{-1} in 10.0 mg mL^{-1} Eth/l.0 M Na_2SO_4 and 10.0 mg mL^{-1} Xyl/l.0 M Na_2SO_4 solution in a voltage range from -1.9 to -1.0 V.

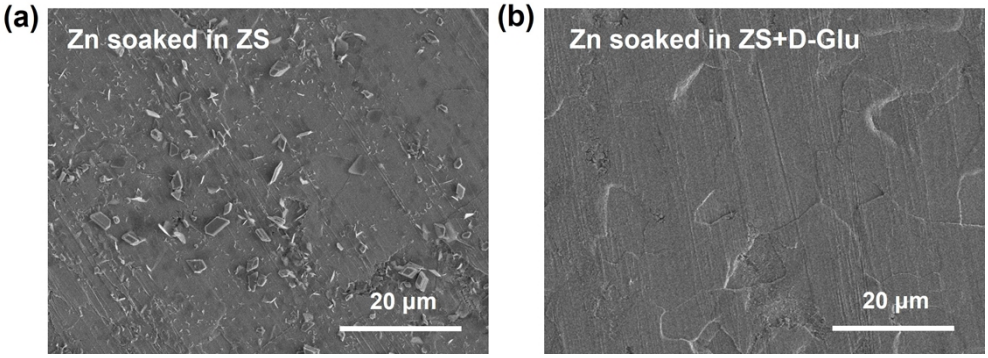

Fig. S16. SEM image of Zn plate soaked in (a) ZS and (b) ZS+D-Glu electrolytes for 7 days.

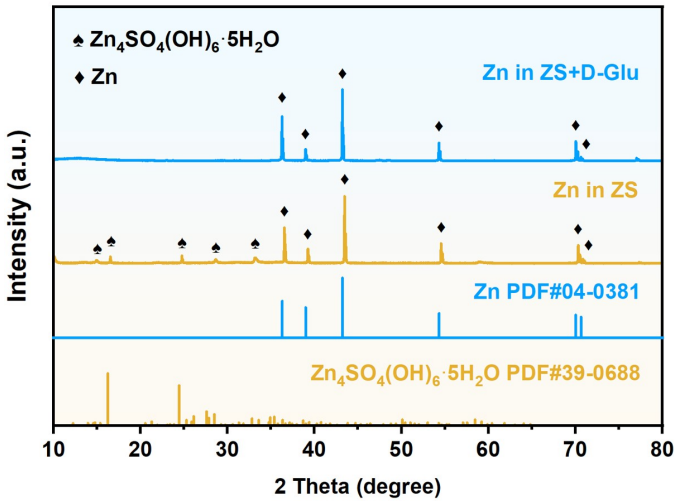

Fig. S17. XRD patterns of the Zn soaked in ZS and ZS+D-Glu for 7 days.

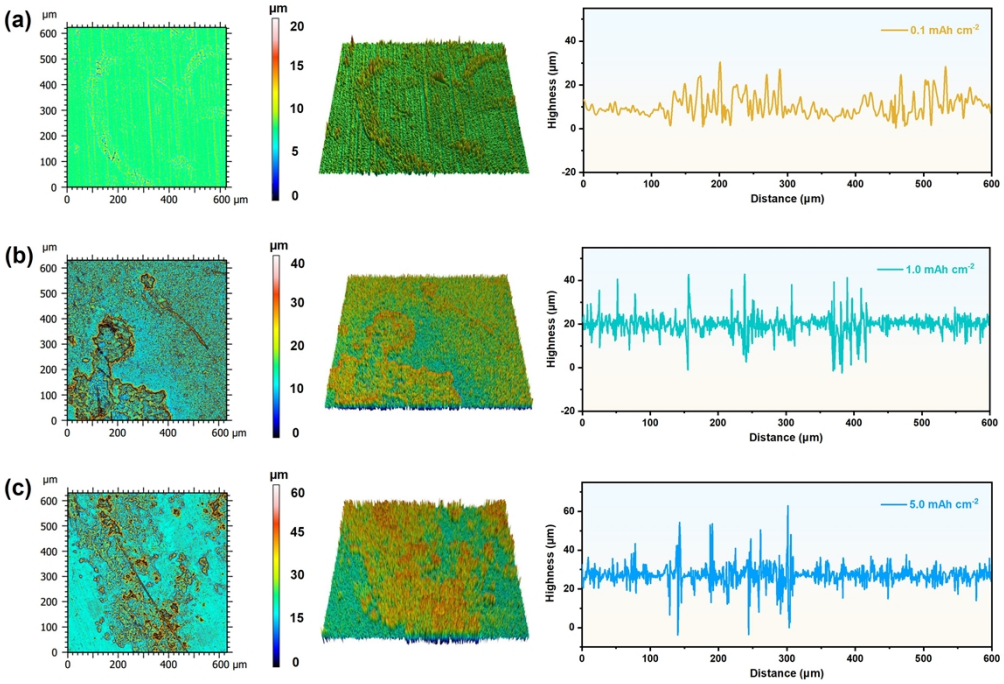

Fig. S18. (a) CLSM optical images of Zn nucleation and deposition process and (b) and the corresponding surface roughness curve of Zn deposition with different capacities from 0.1 to 5.0 mAh cm^{-2} in ZS electrolyte.

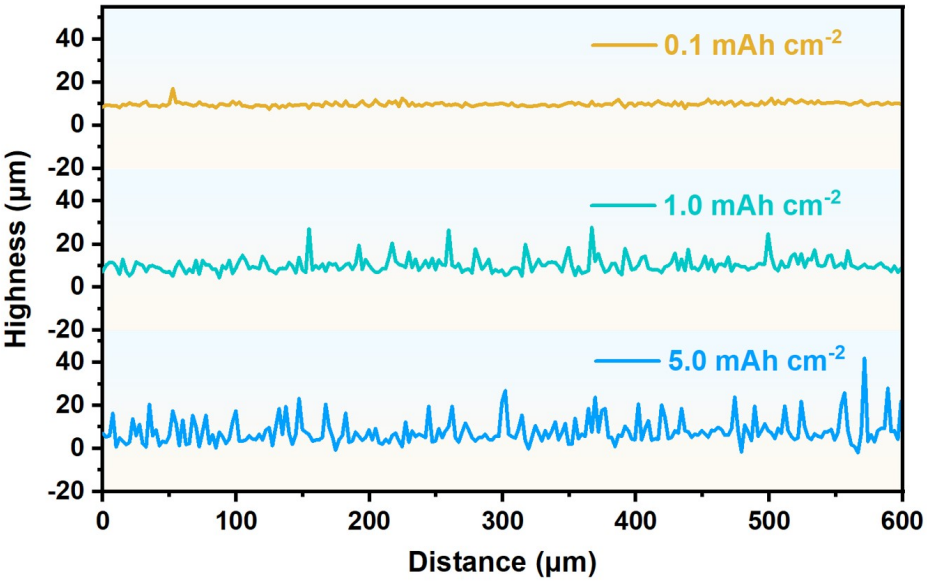

Fig. S19. The corresponding surface roughness curve of Zn deposition with different capacities from 0.1 to 5.0 mAh cm^{-2} in ZS+D-Glu electrolyte.

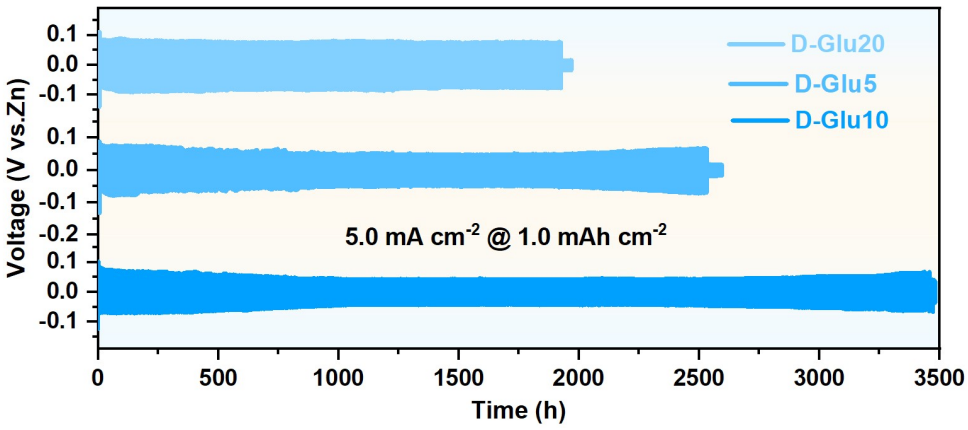

Fig. S20. Voltage-time curves of the Zn||Zn cells with different additive concentrations.

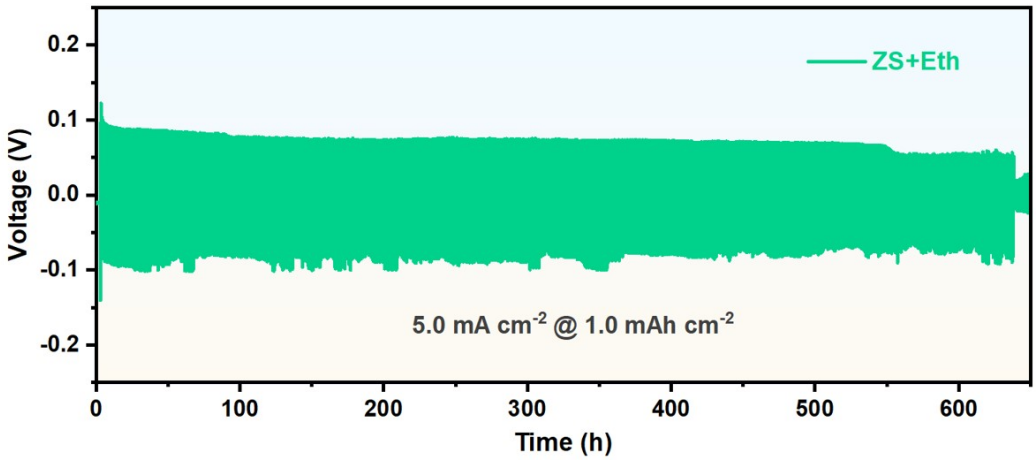

Fig. S21. Cycling tests of the Zn||Zn cells in ZS+Eth electrolytes at 5.0 mA cm^{-2}, 1.0 mAh cm^{-2}.

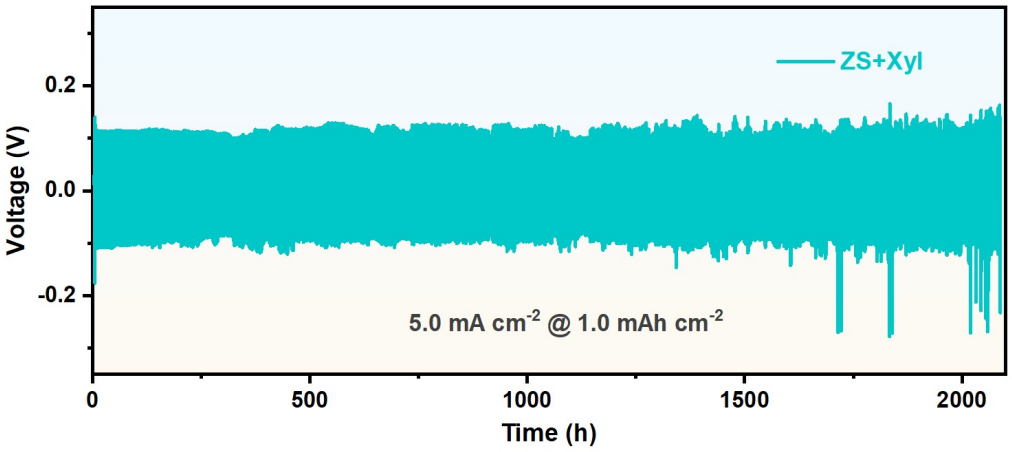

Fig. S22. Cycling tests of the Zn||Zn cells in ZS+Xyl electrolytes at 5.0 mA cm^{-2}, 1.0 mAh cm^{-2}.

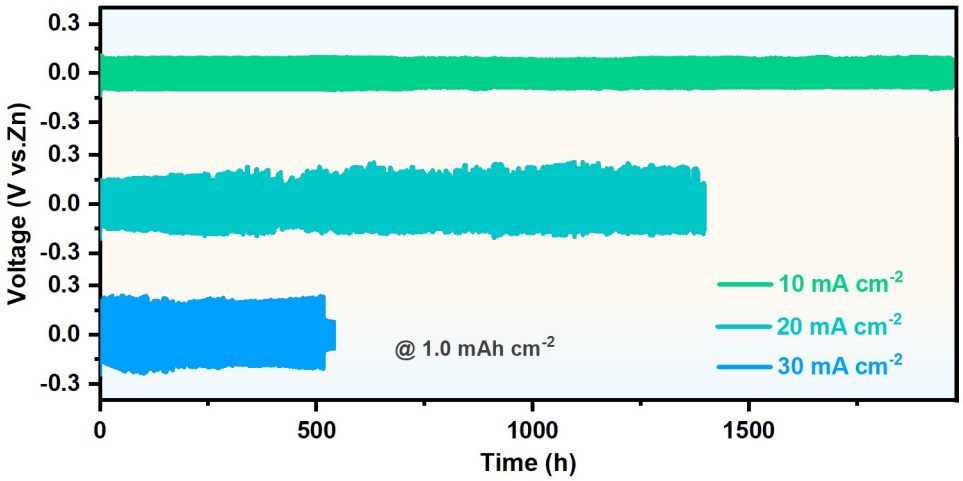

Fig. S23. Cycling tests of the Zn||Zn cells in ZS+D-Glu electrolytes at 10, 20, 30 mA cm^{-2}, 1.0 mAh cm^{-2}.

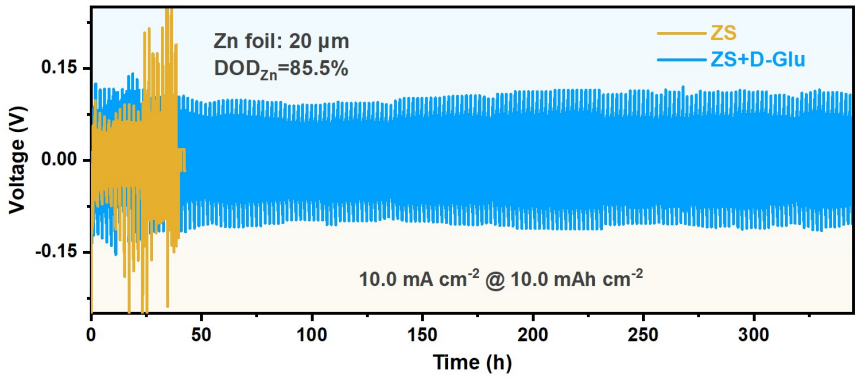

Fig. S24. Cycling tests of the Zn||Zn cells in ZS+D-Glu electrolytes with DOD_{Zn}=85.5%.

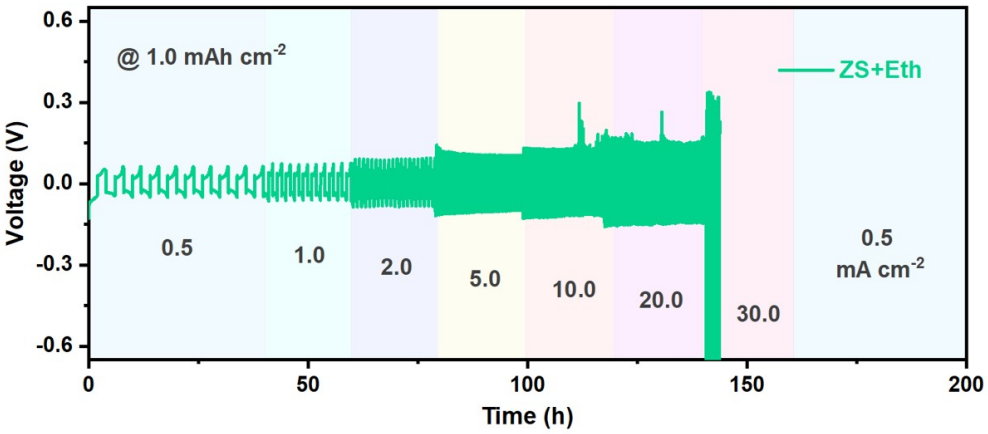

Fig. S25. Rate performance of the Zn||Zn cells in ZS+Eth electrolytes at various current densities with a specific capacity of 1.0 mAh cm^{-2}.

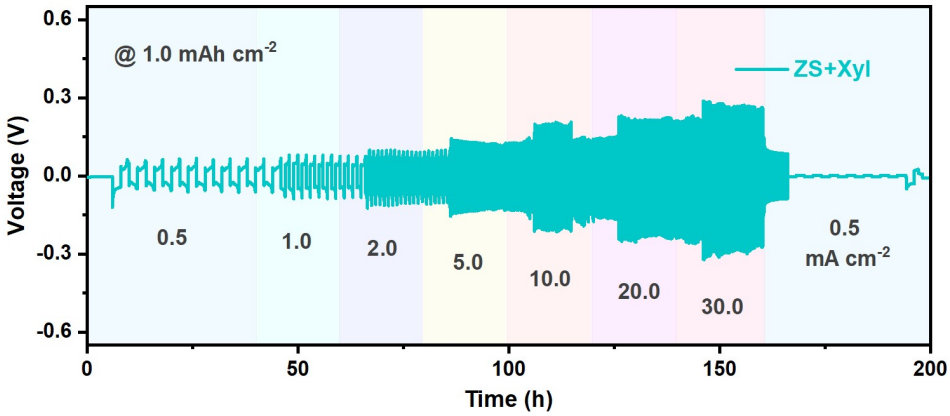

Fig. S26. Rate performance of the Zn||Zn cells in ZS+Xyl electrolytes at various current densities with a specific capacity of 1.0 mAh cm^{-2}.

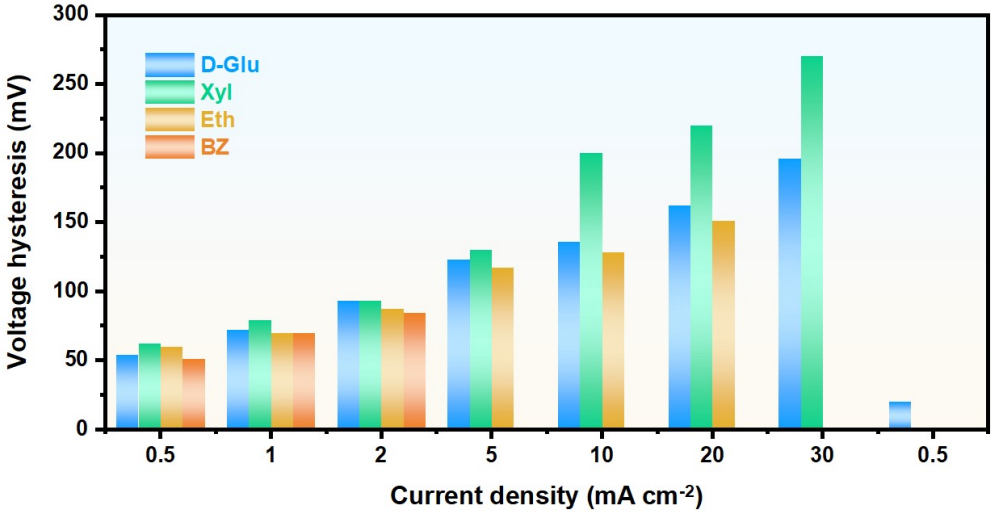

Fig. S27. The overpotential of the Zn||Zn cells in dirrerent electrolytes at various current densities with a specific capacity of 1.0 mAh cm^{-2}.

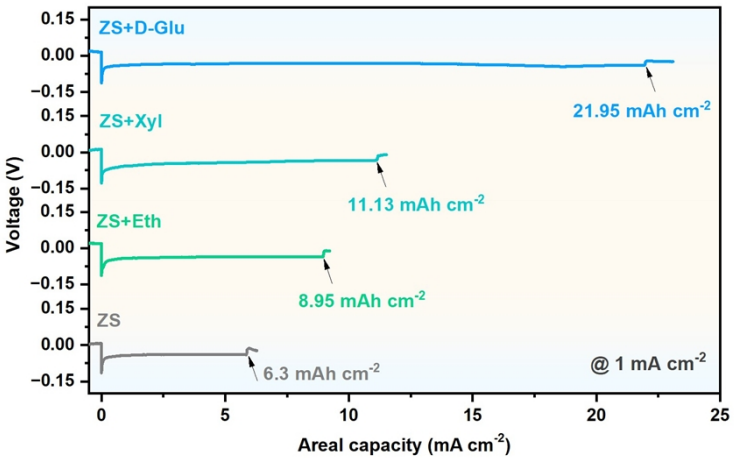

Fig. 28. CAC of Zn electrodes with different electrolytes at 1 mA cm^{-2} current density.

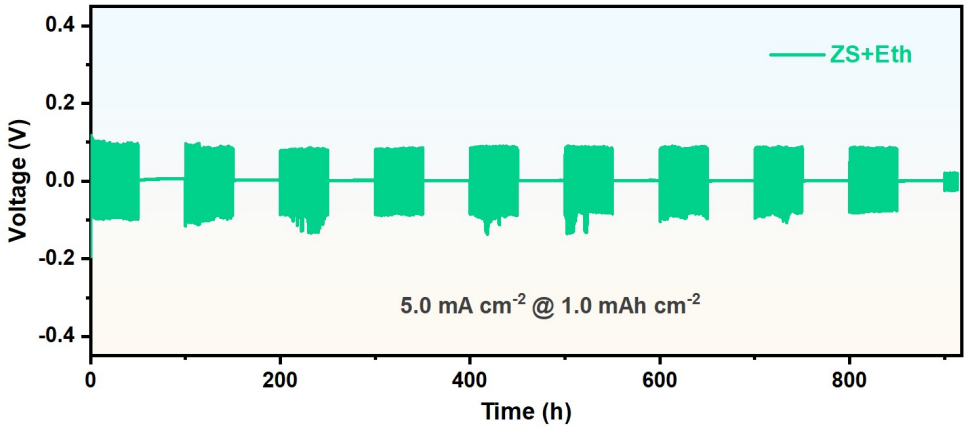

Fig. S29. Shelving-recovery performances of the Zn||Zn cells in ZS+Eth electrolytes at 5.0 mAh cm^{-2} with a specific capacity of 1.0 mAh cm^{-2}.

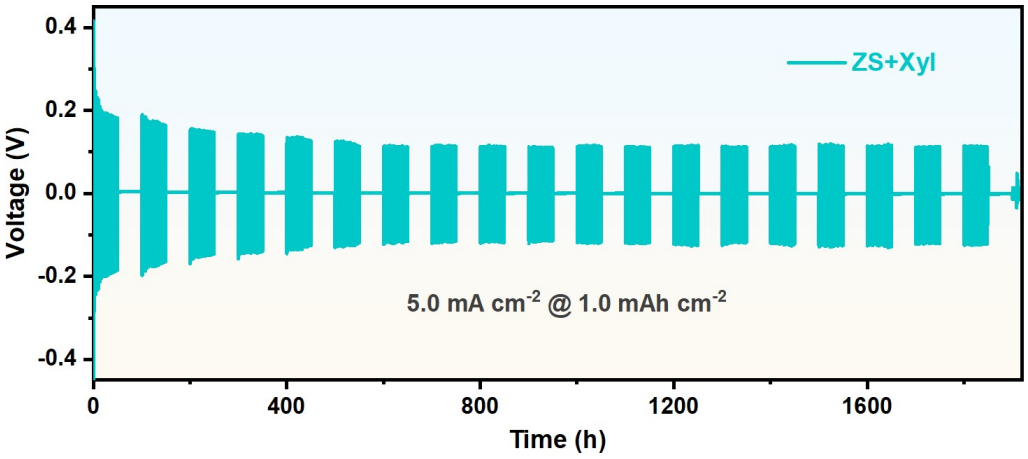

Fig. S30. Shelving-recovery performances of the Zn||Zn cells in ZS+Xyl electrolytes at 5.0 mAh cm^{-2} with a specific capacity of 1.0 mAh cm^{-2}.

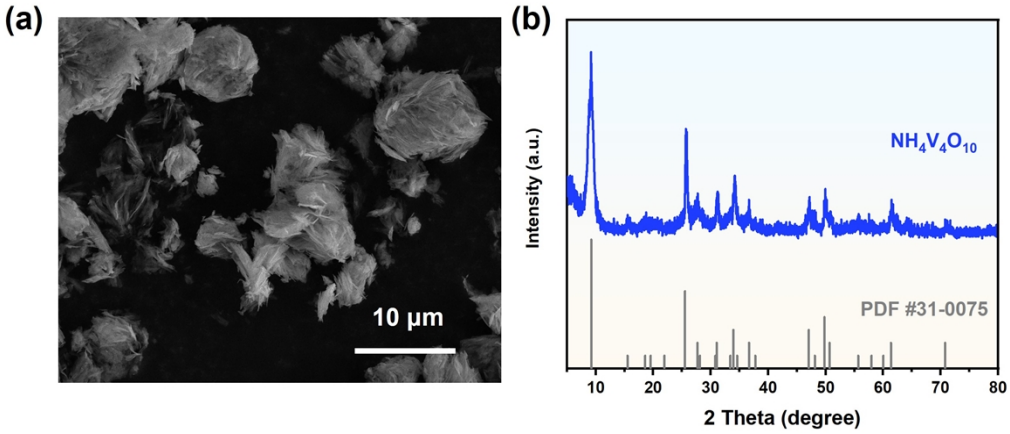

Fig. S31. (a) SEM image and (b) XRD pattern of NVO.

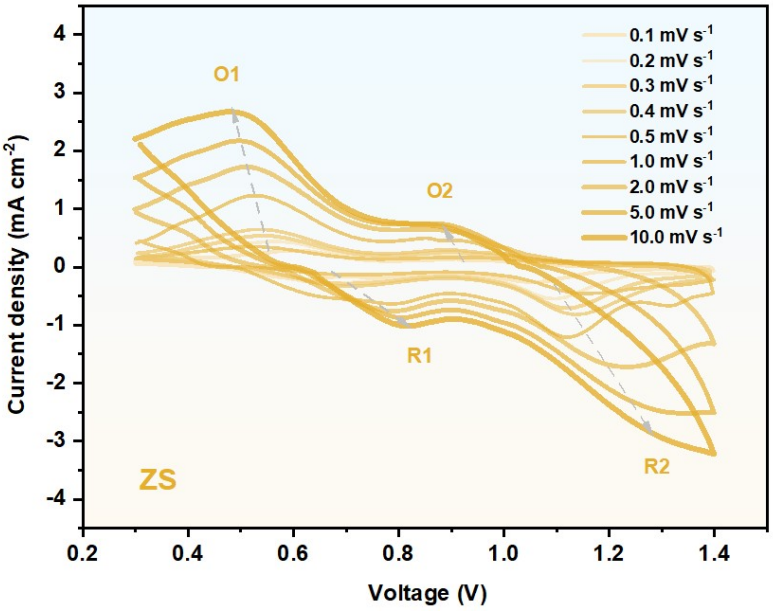

Fig. S32. CV curves of the Zn||NVO full cells using ZS electrolytes measured at different scan rates.

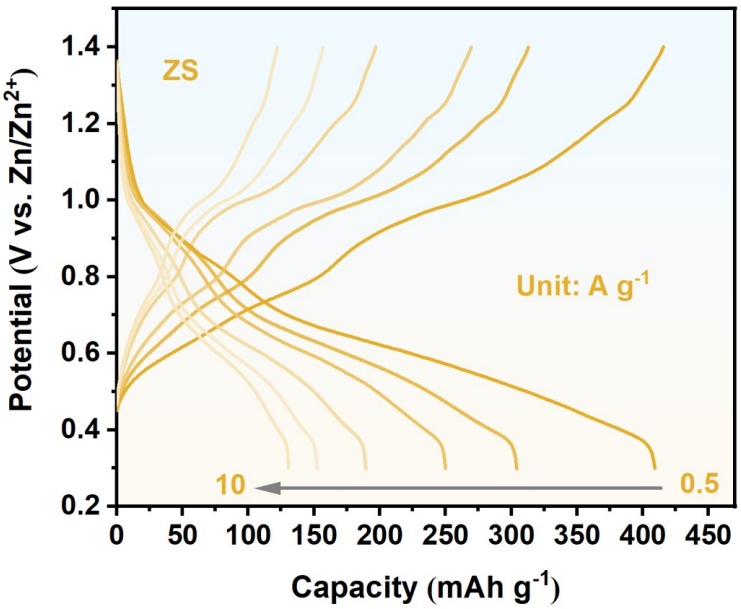

Fig. S33. Charge–discharge profiles of Zn||NVO full cells at various current densities from 0.5 to 10.0 A g^{-1} in ZS electrolytes.

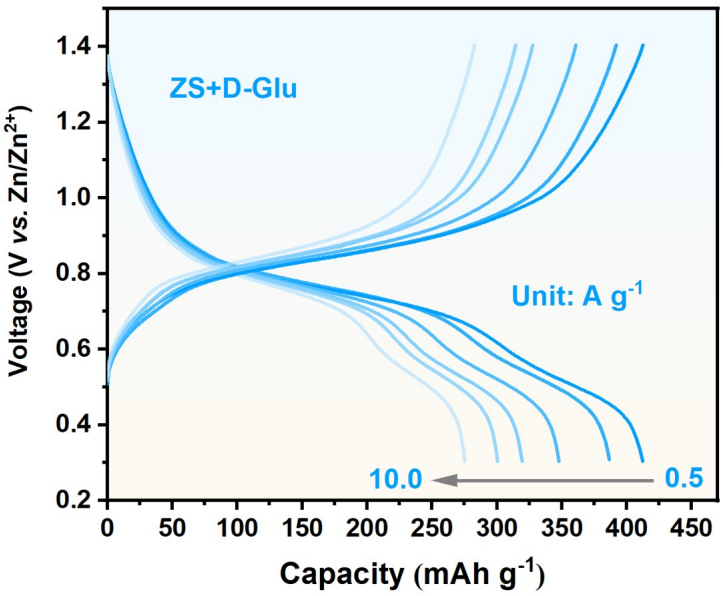

Fig. S34. Charge–discharge profiles of Zn||NVO full cells at various current densities from 0.5 to 10.0 A g^{-1} in ZS+D-Glu electrolytes.

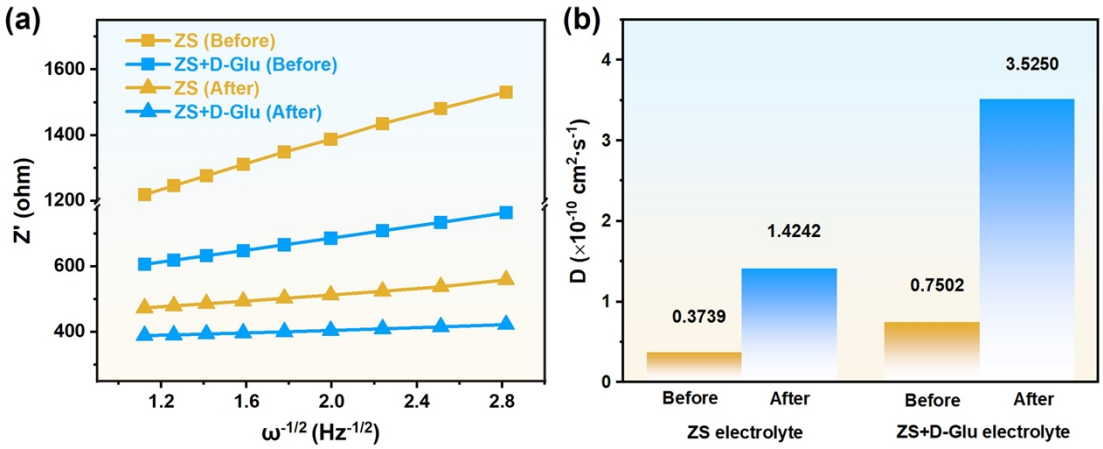

Fig. S35. Linear relationship fitting diagram of Z' and $\omega^{-1/2}$.

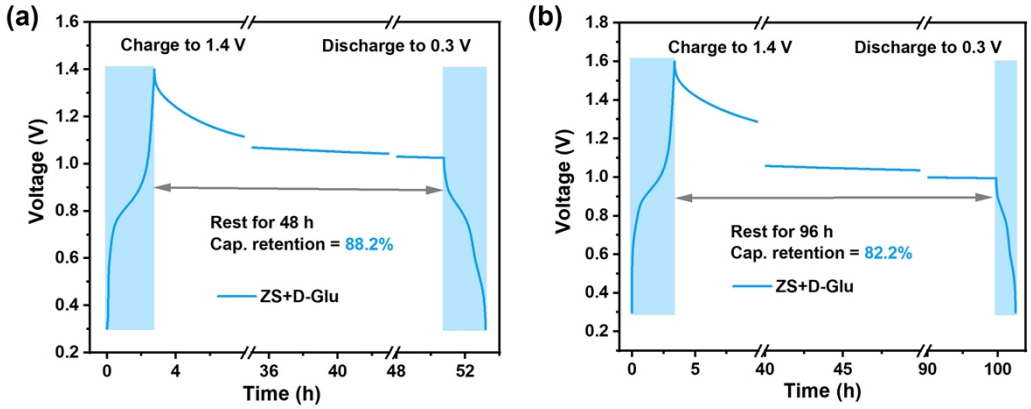

Fig. S36. The capacity retention of Zn||NVO full cells in ZS+D-Glu electrolytes after charging at 1.4 V, resting for (a) 48 h, (b) 96 h, and discharging to 0.3 V.

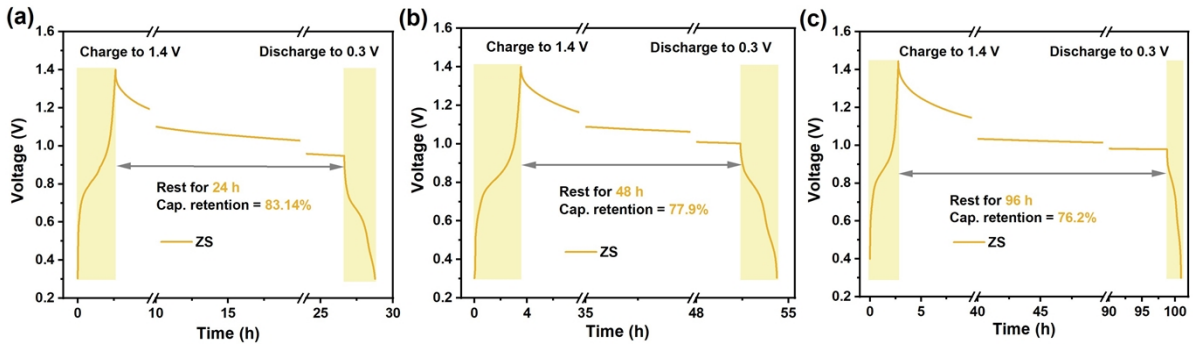

Fig. S37. The capacity retention of Zn||NVO full cells in ZS electrolytes after charging at 1.4 V, resting for (a) 24 h, (a) 48 h, (b) 96 h, and discharging to 0.3 V.

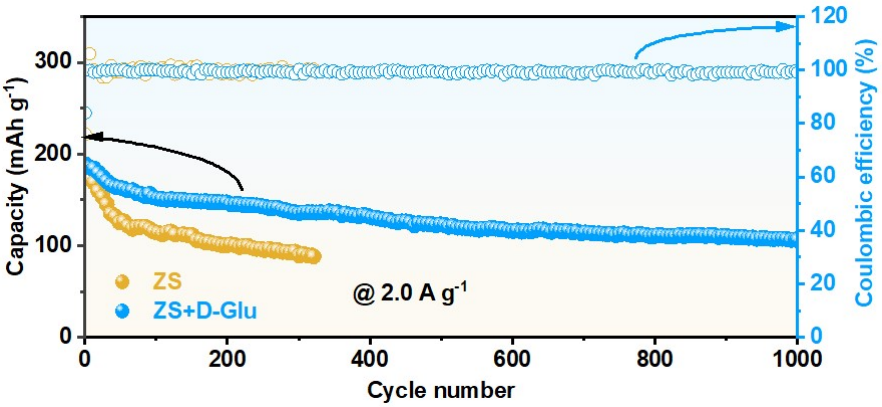

Fig.S38. Cycling performances of Zn||α-MnO_2 full cells in ZS/ZS+D-Glu electrolytes at 2.0 A g^{-1}.

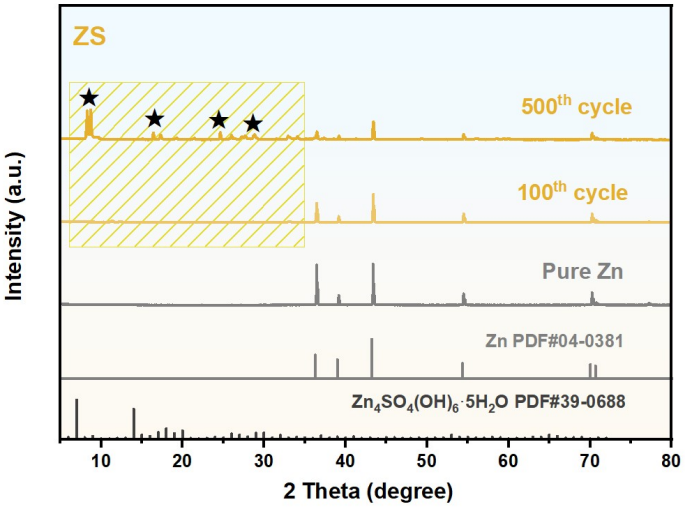

Fig. S39. XRD patterns of Zn||NVO full cells with ZS electrolytes for 100 and 500 cycles.

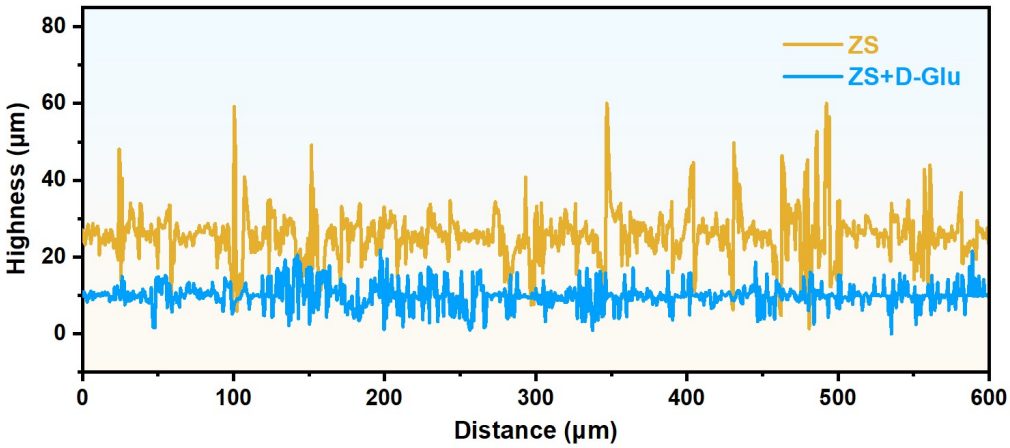

Fig. S40. The corresponding surface roughness curve of the Zn anode cycled in ZS and ZS+D-Glu electrolytes after 100 cycles.

Table S1. CPC comparison of Zn||Zn symmetric cells and CE comparison of Zn||Cu cells using D-Glu with other reported references.

	Electrolyte additive	Zn||Zn symmetric battery			Zn||Cu asymmetric battery			References
		Current density (mA cm^{-2})/Capacity density (mAh cm^{-2})	Lifespan (h)	Cumulative plated capacity (Ah cm^{-2})	Current density (mA cm^{-2})/Capacity density (mAh cm^{-2})	Cycle number	Coulombic efficiency (%)	
1	TFA	5/1	1350	3.375	5/1	720	99.49	Energy Environ. Sci. 2024, 17, 619–629
2	LA	5/5	1080	2.7	1/1	1200	99.89	Angew. Chem. Int. Ed. 2024, e202407261
3	18-crown-6	1/1	1700	0.85	1/0.5	500	99.10	Adv. Energy Mater. 2025, 2404450
4	In-GGE	0.2/0.2	2100	0.21	0.5/0.5	629	98.30	Angew. Chem. Int. Ed. 2024, e202317457
5	BE	1/1	3000	1.5	1/1	1200	99.80	Adv. Funct. Mater. 2024, 2313358
6	ILE	1/1	2400	1.2	1/0.5	2600	99.69	ACS Appl. Mater. 2024, 16, 12544-12553
7	LBG	1/1	1600	0.8	4/4	180	99.60	Energy Environ. Sci. 2025, 18, 1398 – 1407
8	EC	1/1	750	0.375	4/1	300	98.80	ACS Nano. 2024, 18, 27672−27682
9	DTPA	1/1	3100	1.55	2/1	450	99.38	Energy Storage Mater. 2024, 71, 103595
10	SCD	2/1	3900	3.9	2/1	3000	99.62	Energy Environ. Sci., 2025, 18, 1502 – 1513
11	FF	0.5/0.25	2984	0.746	0.5/0.5	370	99.16	Energy Storage Mater. 2025, 74, 103944
12	DA	2/1	1000	1.0	10/1	1000	99.20	Adv. Funct. Mater. 2024, 34, 2316371
13	SDE	1/1	3500	1.75	1/0.5	1800	99.50	Angew. Chem. Int. Ed. 2024, 63, e202411470
14	HIFSI	4/4	2010	4.02	1/0.5	1400	99.70	Nat. Commun. 2024, 15, 4303
15	**D-Glu**	**5/1** **10/5**	**3400** **1920**	**8.5** **9.6**	**1/1**	**2500**	**99.89**	**This Work**

Table S2. EIS fitting results of Zn||Zn cells using ZS/ZS+D-Glu electrolytes before and after cycles.

Electrolyte	Before		After	
ZS	$R_s(\Omega)$=0.2609	$R_{ct}(\Omega)$=1160	$R_s(\Omega)$=0.0131	$R_{ct}(\Omega)$=462.8
ZS+D-Glu	$R_s(\Omega)$=0.2275	$R_{ct}(\Omega)$=575.2	$R_s(\Omega)$=3.116	$R_{ct}(\Omega)$=379.7

Table S3. Comparison of the cycling stability of full cells with previous reports.

Cathode	Electrolyte	Lifespan	References
MnO_2	2M $ZnSO_4$+ 0.1M Gly	0.5 A g^{-1}, 200 cycles	Nano-Micro Lett. 2023, 15:205
α-MnO_2	2M $ZnSO_4$+ 0.2M Gly	2 A g^{-1}, 1000 cycles	Small 2023, 19, 2207502
PANI	1M $ZnSO_4$+ 3M Glycine	1 A g^{-1}, 400 cycles	Adv. Mater. 2022, 34, 2206754
THC	2M $ZnSO_4$+5wt.% Cit	1 A g^{-1}, 1500 cycles	Adv. Funct. Mater. 2024, 2313925
MnO_2	3M $ZnSO_4$+ 0.05M Arg	0.5 A g^{-1}, 200 cycles	Adv. Funct. Mater. 2021, 31, 2103514
CVO	3M $ZnSO_4$+ 10mM TH	4 A g^{-1}, 1000 cycles	Nano Energy 2022, 97, 107145
$NH_4V_4O_{10}$	2M $ZnSO_4$+ L-car	3 A g^{-1}, 1000 cycles	Nano Energy 2024, 132, 110398
ZnHCF	1M $ZnSO_4$+ 10mM Phe	2 A g^{-1}, 1000 cycles	J. Mater. Chem. A, 2024,12, 6610-6622
$NH_4V_4O_{10}$	2M $ZnSO_4$+Gln	1 A g^{-1}, 900 cycles	ACS Nano 2024, 18, 3752−3762
PEDOT-V_2O_5	2M $ZnSO_4$+0.3M Asp	0.05 A g^{-1}, 400 cycles	Adv. Energy Mater. 2023, 13, 2301670
$NH_4V_4O_{10}$	**2M $ZnSO_4$+D-Glu10**	**5 A g^{-1}, 2000 cycles**	**This work**

References

1. X. Jin, G. Lai, X. Xiu, L. Song, X. Li, C. Dai, M. Li, Z. Quan, B. Tang, G. Shao, Z. Zhang, F. Liu, L. Qu, Z. Zhou, *Angew. Chem. Int. Ed.*, 2024, e202418682.
2. S. Zhou, X. Meng, Y. Chen, J. Li, S. Lin, C. Han, X. Ji, Z. Chang, A. Pan, *Angew. Chem. Int. Ed.*, 2024, **63**, e202403050.
3. G. Guo, C. Ji, J. Lin, T. Wu, Y. Luo, C. Sun, M. Li, H. Mi, L. Sun, H.J. Seifert, *Angew. Chem. Int. Ed.*, 2024, **63**, e202407417.
4. D. Li, Y. Tang, S. Liang, B. Lu, G. Chen, J. Zhou, *Energy Environ. Sci.*, 2023, **16**, 3381-3390.
5. R. Wang, J. He, C. Yan, R. Jing, Y. Zhao, J. Yang, M. Shi, X. Yan, *Adv. Mater.*, 2024, **36**, e2402681.
6. T. Ma, Y. Yang, D. Johnson, K. Hansen, S. Xiang, R.M. Thakur, A. Djire, J.L. Lutkenhaus, *Joule*, 2023, **7**, 2261-2273.
7. W. Kohn and L. J. Sham, *Phys. Rev.*, 1965, **140**, A1133-A1138.
8. G. Kresse and J. Furthmüller, *Comput. Mater. Sci.*, 1996, **6**, 15-50.
9. J. P. Perdew, J. A. Chevary, S. H. Vosko, K. A. Jackson, M. R. Pederson, D. J. Singh and C. Fiolhais, *Phys. Rev. B*, 1992, **46**, 6671-6687.
10. G. Kresse and D. Joubert, *Phys. Rev. B*, 1999, **59**, 1758-1775.
11. S. Grimme, J. Antony, S. Ehrlich and H. Krieg, *J. Chem. Phys.*, 2010, **132**, 154104.
12. H. J. Monkhorst and J. D. Pack, *Phys. Rev. B*, 1976, **13**, 5188-5192.
13. V. Wang, N. Xu, J.-C. Liu, G. Tang and W.-T. Geng, *Comput. Phys. Commun.*, 2021, **267**, 108033.
14. A. Thompson, H. M. Aktulga, R. Berger, D. Bolintineanu, W. Brown, P. Crozier, P. in 't Veld, A. Kohlmeyer, S. Moore, T. Nguyen, R. Shan, M. Stevens, J. Tranchida, C. Trott and S. Plimpton, *Comput. Phys. Commun.*, 2021, **271**, 108171.
15. L. Martínez, R. Andrade, E. G. Birgin and J. M. Martínez, *J. Comput. Chem.*, 2009, **30**, 2157-2164.
16. G. A. Kaminski, R. A. Friesner, J. Tirado-Rives and W. L. Jorgensen, *J. Phys. Chem. B*, 2001, **105**, 6474-6487.
17. H. J. C. Berendsen, J. R. Grigera and T. P. Straatsma, *J. Phys. Chem.*, 1987, **91**, 6269-6271.